Flight Test Preparation of an Ultra-Low Ballistic Coefficient Entry Vehicle

Kassandra Perez-Rivera[1] and David L. Akin[2]
Space Systems Laboratory, University of Maryland, College Park MD, 20742, USA

This paper presents the adaptation of ParaShield, an ultra-low ballistic coefficient (ULβ) entry vehicle concept developed at the University of Maryland's Space Systems Laboratory, for an experimental suborbital flight test under NASA's RockSat program. Ultra-low ballistic coefficient entry vehicles with β less than 300 Pa experience significantly reduced peak stagnation point temperatures and heating rates, enabling the use of simplified thermal protection systems. ParaShield is a ULβ entry vehicle design that utilizes a deployable radiative heat shield constructed from high-temperature ceramic fabrics supported by an umbrella-like mechanical framework. Because the heat shield is decoupled from the spacecraft body, the payload is no longer constrained to a traditional conical geometry, allowing for greater flexibility in payload configuration and mission design. Adapting ParaShield to the RockSat mission architecture introduces a new set of constraints including payload envelope limitations, mass requirements, deployment timing, and initial flight conditions. This paper presents the system-level design refinements required to meet these constraints, including updates to vehicle geometry, mass distribution, and trajectory analysis for the nominal flight environment. Results demonstrate that the ParaShield design shows strong potential to be configured as a flight-ready experimental payload within the RockSat program guidelines. This suborbital flight test represents a low-cost opportunity to experimentally validate ParaShield's entry behavior, informing future scaling efforts and advancing deployable thermal protection systems for atmospheric entry applications.

I. Nomenclature

A	=	Area of Heat Shield, m^2
D	=	Drag Force, N
d	=	Thickness of Heat Shield Fabric, m
h	=	Altitude, m
k	=	Sutton-Graves Constant
k_{fabric}	=	Thermal Conductivity of Heat Shield Fabric, W/(m · °C)
L	=	Lift Force, N
L/D	=	Lift-to-Drag Ratio
m	=	Vehicle Mass, kg
Q	=	Heat Load, J/m^2
q	=	Dynamic Pressure, Pa
$\dot{q}$	=	Heat Rate, W/m^2
R	=	Radius of the Heat Shield, m
T	=	Temperature, °C
TPS	=	Thermal Protection System
t	=	Time, s
V	=	Velocity, m/s
V_c	=	Orbital Velocity, m/s

[1] Undergraduate Researcher, Department of Aerospace Engineering, AIAA Student Member 1869368
[2] Director, Space Systems Laboratory. Professor, Department of Aerospace Engineering, AIAA Senior Member

β	=	Ballistic Coefficient, Pa
ULβ	=	Ultra-Low Ballistic Coefficient
γ	=	Flight Path Angle, deg.
ε	=	Emissivity of Heat Shield Fabric
ρ	=	Density, kg/ m^3
σ	=	Stefan-Boltzmann Constant, W/(m$^2 \cdot$ K^4)

II. Introduction

As the United States returns to the Moon with the Artemis program, there is an ever-growing demand for reliable entry vehicles for both crewed and uncrewed applications. The design of these entry vehicles has traditionally been constrained by the launch vehicle geometry, and ballistic coefficients ($\beta = m/C_D A$) have historically fallen in the range of 2500–5000 Pa[3] [1]. At this range of β, aerodynamic heating produces extremely high stagnation-point heating which requires the use of heavy, single-use ablative thermal protection systems (TPS).

An alternative design approach was developed by graduate students at MIT in Fall 1988 and later pursued by the University of Maryland's Space Systems Laboratory (SSL), in which the ballistic coefficient is treated as a primary design parameter rather than a consequence of launch vehicle constraints. When β is reduced to the range of 150–300 Pa, peak stagnation-point temperatures and heating rates decrease substantially, enabling the use of reusable ceramic fabric as the thermal protection system [2]. At these ultra-low ballistic coefficients (ULβ), a deployable radiative heat shield supported by an umbrella-like mechanical framework can be packaged compactly during launch and deployed prior to atmospheric entry. Because the heat shield is decoupled from the spacecraft body, the spacecraft itself is no longer constrained to a conical shape which allows for arbitrary payload shapes and broader mission flexibility.

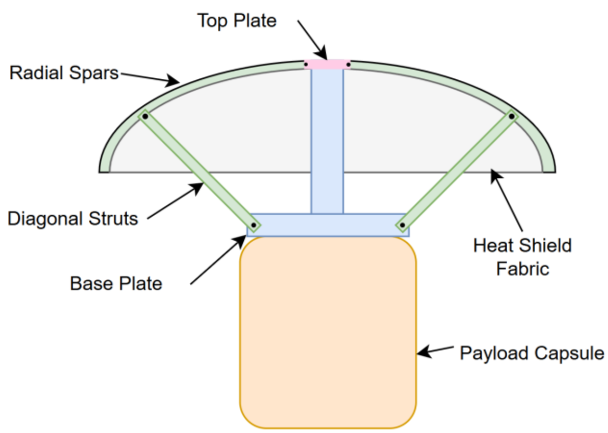

Fig. 1: ParaShield Concept Sketch

This vehicle design is referred to as ParaShield, as the deployable fabric structure serves as both the primary thermal protection system during entry and as a terminal deceleration device during descent. Several studies have examined ParaShield through analytical modeling, wind tunnel testing, computational fluid dynamics, and limited flight hardware development [1-4]. These studies established theoretical feasibility and performance advantages for a range of applications, from low Earth orbit cargo return to lunar and Mars returns [1, 2]. Despite this analytical foundation, the concept has not yet been validated through a flight test.

This paper presents the adaptation of the ParaShield concept in preparation for a suborbital flight test under NASA's RockSat program. The RockSat mission architecture imposes a new set of constraints including payload envelope limitations, mass and center-of-gravity requirements, deployment timing, and initial flight conditions set by the Terrier-Improved Malemute sounding rocket. Meeting these constraints requires refinement of vehicle geometry, design of a deployment mechanism, and mass distribution. The objective of this paper is to demonstrate that ParaShield can be configured as a flight-ready experimental payload within the constraints of the RockSat mission. The NASA RockSat flight test provides a low-cost opportunity to obtain experimental data on ParaShield to validate analytical models for potential future orbital and planetary entry applications.

[3] The ballistic coefficient is commonly expressed in kg/m^2. In this paper, β is expressed in Pascals to maintain consistency with previous ParaShield studies.

III. Foundational Theory

The entry dynamics and heating analysis presented in this section are characterized by three vehicle parameters, the ballistic coefficient β, lift-to-drag ratio *L/D*, and the heat shield radius *R*. The ballistic coefficient is the central design parameter for ULβ entry vehicles and is defined as:

$$\beta = \frac{m}{C_D A} \tag{1}$$

The *L/D* is treated as a constant input that is determined by the magnitude of the center-of-mass offset from the vehicle geometric centerline.

A. Atmospheric Entry Dynamics

The dynamics of ParaShield during atmospheric entry are modeled as a three-degree-of-freedom point mass. The state vector is defined by altitude h, speed *V*, and flight path angle γ. The flight path angle is measured relative to the local horizon, where a positive flight path angle corresponds to an ascending trajectory and a negative angle corresponds to a descending trajectory. The equations of motion during entry are:

$$\frac{dh}{dt} = V \sin\gamma \tag{2}$$

$$\frac{dV}{dt} = -\frac{D}{m} - g\sin\gamma \tag{3}$$

$$\frac{d\gamma}{dt} = \frac{1}{V}\left(\frac{L}{m} - \left(1 - \frac{V^2}{V_c^{\,2}}\right) g\cos\gamma\right) \tag{4}$$

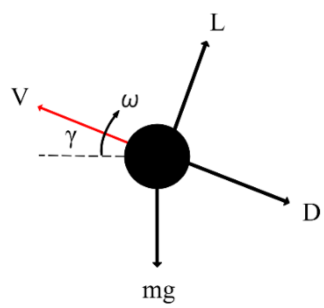

Fig. 2: Free Body Diagram of ParaShield During Atmospheric Entry

To fully simulate the entry trajectory, gravitational acceleration and atmospheric density are modeled as functions of altitude. Gravitational acceleration varies according to the inverse-square law

$$g(h) \;=\; g_0\left(\frac{R_e}{R_e + h}\right)^2 \tag{5}$$

where $g_0 = 9.80665\ \frac{m}{s^2}$ and $R_e = 6378$ km. Atmospheric density is modeled as an exponential where $\rho_0 = 1.226\ \frac{kg}{m^3}$ and H = 7524 m [5].

$$\rho(h) \;=\; \rho_0 e^{-h/H} \tag{6}$$

To quantify the total deceleration experienced during entry, the drag and lift accelerations are calculated. Lift is generated by offsetting the center-of-mass from the vehicle geometric centerline, inducing an asymmetric pressure distribution over the surface of the heat shield. The resulting drag and lift accelerations are:

$$\frac{D}{m} = \frac{q}{\beta} \tag{7}$$

$$\frac{L}{m} = \frac{D}{m}\left(\frac{L}{D}\right) \tag{8}$$

where dynamic pressure is $q = \frac{1}{2}\rho(h)V^2$. The total deceleration on the vehicle is then:

$$n = \frac{\sqrt{\left(\frac{D}{m}\right)^2 + \left(\frac{L}{m}\right)^2}}{g_0} = \frac{q}{\beta}\frac{\sqrt{1 + \left(\frac{L}{D}\right)^2}}{g_0} \tag{9}$$

The peak value of deceleration is expected to occur near maximum dynamic pressure and defines the maximum structural load the vehicle must withstand, driving structural system design. With the entry trajectory established, the resulting heating environment can be characterized.

B. Aerodynamic Heating

During atmospheric entry, the kinetic energy of the entry vehicle is converted to thermal energy as the surrounding air is compressed and decelerated across the bow shock. The thermal analysis presented here focuses on the stagnation point heating environment, which represents the point of maximum heat flux on the heat shield and is the conservative design case for TPS sizing. The stagnation point heating rate is estimated using the Sutton-Graves approximation

$$\dot{q}_s = k\sqrt{\frac{\rho}{R}}V^3 \tag{10}$$

where k = 1.7415× 10^{-4} for flight through Earth's atmosphere [6]. Stagnation heating rate is inversely proportional to heat shield radius, as a blunter body will produce a stronger detached shock and more thermal energy will go into the vehicle wake rather than the vehicle surface. The Sutton-Graves formula assumes a laminar boundary layer and a fully catalytic wall, both of which are conservative assumptions that will overpredict heating.

The peak surface temperature reached by the heat shield is another critical quantity bounding the TPS design. It is conservatively estimated by neglecting convective cooling, assuming radiative equilibrium, as conductive and convective cooling effects are neglected [3]. The heat flux across the shield varies throughout the entry trajectory, but peak heating conditions are treated using a quasi-steady energy balance, which is a standard and conservative simplification [6].

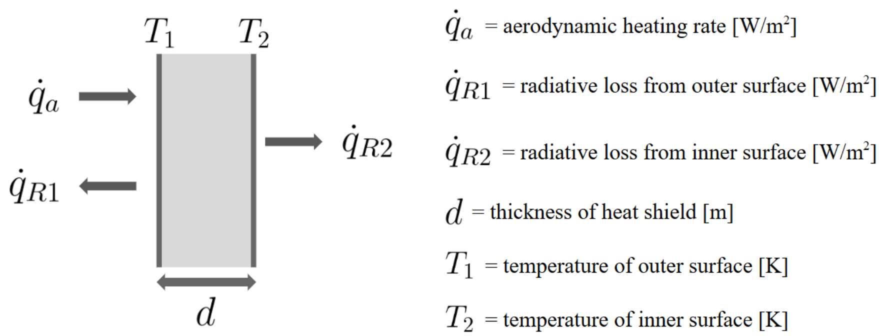

Fig. 3: Heat Flux Model of Heat Shield

The energy balance at the outer boundaries of the heat shield surface is:

$$\dot{q}_a = \dot{q}_{R1} + \dot{q}_{R2} \tag{11}$$

where $\dot{q}_R$ represents heat flux from radiation and $\dot{q}_a$ represents heat flux from aerodynamic heating. The stagnation point heat flux $\dot{q}_s$ is taken as the predicted worst case aerodynamic heating. The heat conducted through the fabric to the inner surface will be equal to the heat radiated from the inner surface:

$$\dot{q}_{cond} = \dot{q}_{R2} \tag{12}$$

Substituting Eq. (12) into Eq. (11) and expanding the heat flux terms yields:

$$\dot{q}_s = \varepsilon_1\sigma {T_1}^4 + \frac{k_{fabric}}{d}(T_1 - T_2) = \varepsilon_2\sigma {T_2}^4 \tag{13}$$

Where T_1 and T_2 are the outer and inner surface temperatures, and ε_1 and ε_2 are emissivities of the outer and inner fabric surfaces respectively. Equation (13) will be solved at the stagnation point numerically for increasing fabric layer counts until the predicted inner surface temperature is below the continuous use temperature limit of the selected structural material. Lastly, the total heat load is found by integrating the stagnation point heating rate over the entry trajectory.

$$Q = \int_0^{t_f} \dot{q}_s\, dt \tag{14}$$

Equation (14) is evaluated numerically over the entry trajectory using trapezoidal integration. All three of these quantities drive different aspects of the TPS design. The peak heating rate governs the maximum surface temperature, setting the continuous use temperature rating for the heat shield material. The maximum inner surface temperature constrains the structural spar material selection. The total heat load drives the required fabric thickness and TPS mass as it determines how much energy must be absorbed or re-radiated over the descent.

IV. RockSat Mission Overview

The ParaShield flight experiment is designed for a suborbital flight under the NASA RockSat program, which provides college teams the opportunity to design and fly experiments aboard a Terrier-Improved Malemute two-stage sounding rocket. Following the second stage burn out, the skin and nose cone are ejected, exposing all onboard experiments to space. At apogee, the sounding rocket nominally reaches an altitude of 160 km, a velocity of 300 m/s, and a flight path angle of 0°. For the ParaShield experiment, the sounding rocket flight profile defines the initial conditions for atmospheric entry and the mechanical and structural constraints imposed during ascent.

A. System Requirements

The RockSat program imposes a strict set of constraints on all payloads, which can be translated into system-level design requirements for the ParaShield experiment [7]. These requirements span four categories mechanical, thermal, electrical, and operational.

Table 1: Top-Level System Requirements

Requirement ID	Requirement
L1-001	The system shall weigh 13.6±0.45 kg (includes the deck weight which is ~1.5 kg)
L1-002	The system shall withstand 25 g in all three axes and up to 50 g in the Z axis
L1-003	The system shall fit inside of the 0.3 m (12 in.) diameter and 0.27 m (10.75 in.) tall envelope
L1-004	All deployments/ejections must deploy at a speed less than 0.025 m/s (1 in/s)
L1-005	The system center-of-gravity shall remain within 0.025 m (1 in.) of the deck center (X-Y)
L1-101	The system onboard RockSat and ParaShield shall withstand at least 232 °C
L1-201	The system shall use less than 3.75 A across all power connections
L1-202	The system shall interface via standard 15-pin RockSat power connector
L1-203	The system on-board RockSat shall operate on the 1 Ah battery
L1-301	The system shall survive water splashdown and exposure to saltwater
L1-302	The system shall operate autonomously until system shut down (~332 seconds)

The mechanical requirements (L1-001 through L1-005) impose the largest constraints on the ParaShield design. The 0.3 m diameter payload envelope (L1-003) directly limits the maximum deployable heat shield area, setting the floor on the achievable ballistic coefficient. The center-of-gravity constraint (L1-005) is significant because the internal center-of-mass offset from the vehicle centerline is the mechanism by which *L/D* is generated during entry. The 0.025 m X-Y plane limit complicates the overall ParaShield packing logistics and achievable center-of-mass offsets. The launch load requirement (L1-002) will likely govern the structural sizing of the structural system and deployment mechanism. The payload mass requirement (L1-001) constrains the overall system design to a total mass of 12.1 kg, including ParaShield and any supporting components onboard RockSat.

The thermal requirement (L1-101) establishes a minimum material performance all onboard systems must satisfy. The ParaShield heat shield will comfortably exceed this minimum, but it may be a factor when designing the electronics that will stay onboard RockSat. These system-level requirements ensure that the ParaShield design will be able to survive the rigors of launch, operate autonomously, and collect meaningful data during the flight test.

B. Deployment Timing Trade Study

To determine the design specifications ParaShield must withstand, such as peak thermal and structural loads, the expected conditions throughout atmospheric entry must be modeled. The deployment timing of ParaShield separating from the RockSat rocket is a critical design decision as it directly sets the initial conditions for atmospheric entry. The equations of motion of atmospheric entry require three initial conditions: altitude h_0, velocity V_0, and flight path angle γ_0. Each of these quantities change throughout RockSat's flight and will alter the resulting entry trajectory of ParaShield. Variations in these initial conditions propagate into differences in peak deceleration, peak stagnation heating rate, and total heat load. Therefore, a trade study was conducted to analyze the differences in entry conditions between various deployment timings.

The valid deployment window is constrained at both ends by the RockSat mission timeline. The aft skin separation occurs at t = 81 s, and prior to this event the payloads remain enclosed within the rocket skin. The latest possible deployment is at t = 336 s, when power to the experiments is shut off. This defines a valid deployment window of 255 seconds which spans across ascent, apogee, and descent.

NASA provided a RockSat mission timeline containing 15 timestamped events across this window, each providing nominal altitude, velocity, and flight path angle. Due to the lack of higher-resolution data, each of these 15 events was treated as a potential deployment case and used as initial conditions for the entry equations of motion. For each case, the three-degree-of-freedom entry equations were integrated using MATLAB's ODE45.

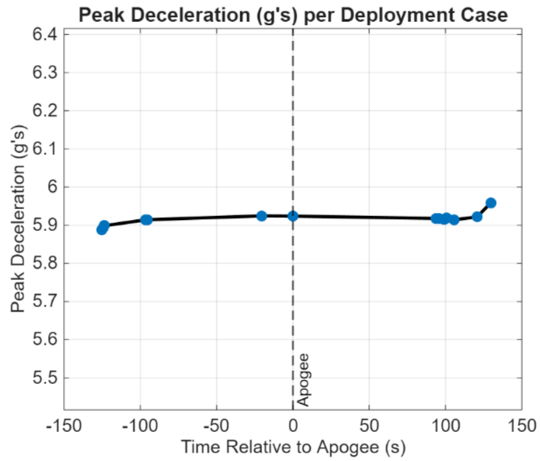

Fig. 4: Peak Deceleration vs Relative Time for All Cases

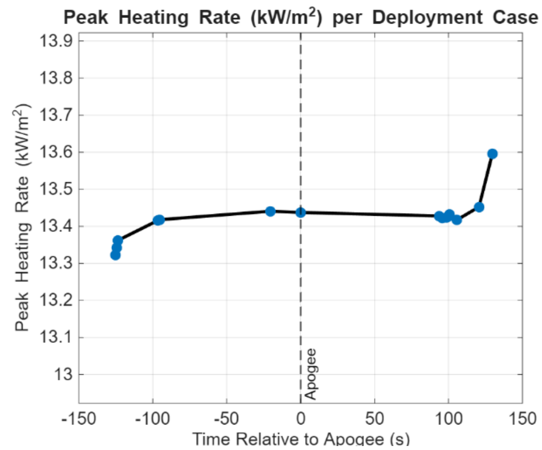

Fig. 5: Peak Heating Rate vs Relative Time for All Cases

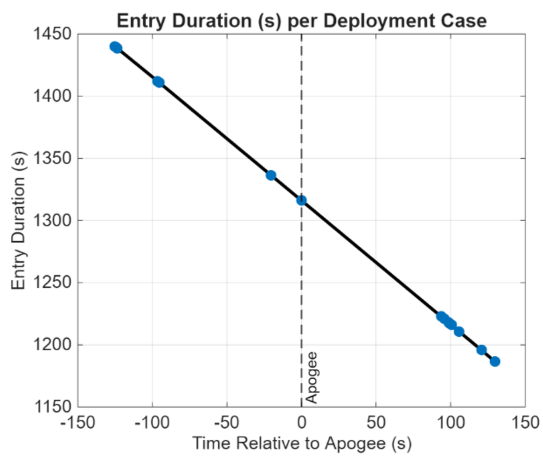

Fig. 6: Entry Duration vs Relative Time for All Cases

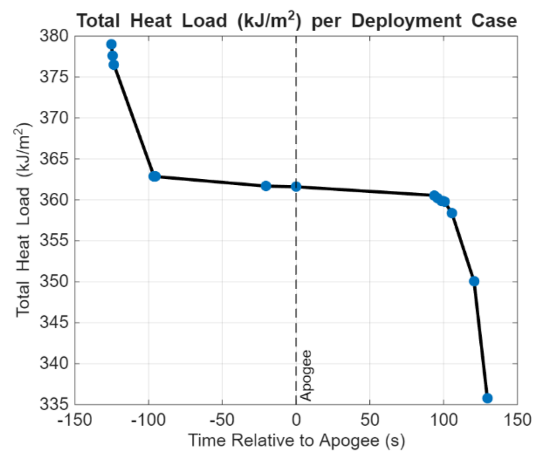

Fig. 7: Total Heat Load vs Relative Time for All Cases

The trade study revealed that peak deceleration and peak stagnation point heating rate were nearly identical across all deployment cases, converging to an average of 5.9 g and 13.4 kW/m^2, respectively, as shown in Figs. 4 and 5. This insensitivity arises because peak aerodynamic loads occur at the same altitude band regardless of when the vehicle is released. Total heat load converges to approximately 361 kJ/m^2 around apogee, but either increases or decreases depending on the relative time, which is expected as Q represents accumulated heating over the flight time.

The meaningful differentiator between deployment cases is entry duration, shown in Fig. 6, with flight duration ranging between 1440 s and 1190 s for the first and last deployment cases. Apogee deployment yields a flight duration of 1320 s and is the only point during the RockSat flight profile that the rocket's spin rate will approximately be 0 Hz [7], reducing the risk of deployment complications. Therefore, apogee is selected as the nominal deployment time.

It should be noted that this analysis was conducted using assumed design values of β = 100 Pa, L/D = 0.2, R = 0.25 m, and m = 10 kg, which represent first-pass estimates rather than finalized values. This creates a circular dependency in the design process: the equations of motion require β as an input, but β cannot be known until the structural and thermal protection designs are completed, which they themselves depend on the entry conditions predicted by the equations of motion. This is resolved through design iteration, as the values assumed here represent a first pass of this loop. As the vehicle design matures and a more precise β is established, the entry analysis is updated, and results are checked for consistency with the initial assumptions.

C. Entry Conditions and Design Requirements

Now that the nominal deployment time is set at apogee, the three-degree-of-freedom entry equations were integrated for a design case of β = 219 Pa, L/D = 0.2, R = 0.36 m, and m = 11.8 kg to define the aerodynamic and thermal conditions ParaShield must withstand. These values were found through structural and TPS design iterations, only the converged design is presented in this paper.

Table 2: Entry Conditions for Estimated Design Values (β = 219 Pa, L/D = 0.2, R = 0.36 m, m = 11.8 kg)

Parameter	Value
Peak Deceleration	6.22 g
Peak Dynamic Pressure	1330 Pa
Peak Velocity	1342 m/s
Splashdown Velocity	18.7 m/s
Peak Stagnation Point Heating Rate	18.1 kW/m^2
Peak Surface Temperature	505 °C
Total Heat Load	474 kJ/m^2
Entry Duration	914 s

V. ParaShield Vehicle Design

A. Geometry

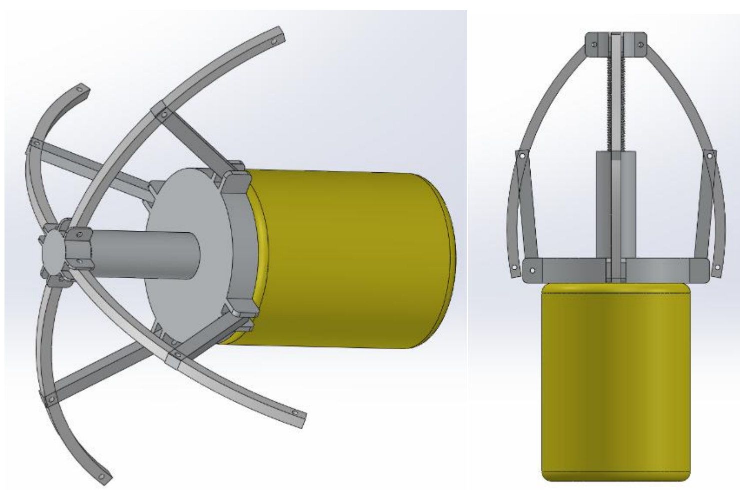

Fig. 8: ParaShield In-Flight Configuration (Left), ParaShield Stored Configuration (Right)

The structural system of ParaShield consists of four main components. The set of radial spars that support the flexible heat shield fabric, the diagonal struts that support the spars, top and bottom plates, and the center support column that protects the lead screw and connects to the payload section (also demonstrated in Fig. 1). The heat shield fabric (not shown in Fig. 8) is stretched across the radial spars, which are arranged symmetrically about the central support column and deployed outward to form a spherical cap geometry. The spherical cap shape is chosen to provide a favorable pressure distribution over the heat shield during entry. The diagonal struts help brace the spars against the aerodynamic and structural loads experienced during entry. The payload capsule is mounted behind the heat shield, protected in the wake of the TPS and structural systems. The system is drove by a linear screw that extends out the radial spars and allows the system to fit into the small RockSat payload envelope. Upon deployment at apogee, the spars swing outward and the diagonal struts hold them in place, keeping the heat shield fabric in the deployed configuration.

The relative geometric design of ParaShield has already been established, but refinements had to be made to scale down the ParaShield design to the RockSat payload envelope. The final geometric values such as shield radius, arc central angle, and shield area are shared in the design summary in Section V.D.

B. Heat Shield Material Selection

When choosing the material to use for the ParaShield heat shield there were four major considerations. First, the heat shield material must have a sufficient continuous use temperature limit that can withstand the predicted maximum surface temperature that will be experienced during entry. The material must have a high emissivity to re-radiate the incoming aerodynamic heating. The material must have low thermal conductivity to limit heat conducted to the inner surface and thus the supporting structure. Lastly, the material should have low density to reduce overall TPS mass and remain within the limited RockSat mass budget.

The possible heat shield materials were restricted to the 3M Nextel family of ceramic fabrics due to past use in heat shield designs, material flexibility, and extensive technical data available online. The advantage of using these ceramic fabrics is that they can be cut, layered, and attached to the umbrella-like framework without specialized manufacturing processes. There were four primary 3M Nextel fiber compositions that were considered for this design: 312, 440, 610, and 720. Nextel 610 and 720 are considered structural compositions that have increased tensile strength but reduced continuous use temperature ratings and lack of published thermal data [8]. Therefore, the material trade study was limited to the Nextel 312 and 440 compositions. Thermal properties for both remaining fabric compositions were obtained directly from the 3M Nextel Technical Reference Guide (Ref. [8]) and are summarized in Table 3.

Table 3: 3M Nextel 312 and 440 Comparison

Fabric	Emissivity (ε)	Thermal Conductivity (W/m°C)	Continuous Use Temperature (°C)	Areal Weight (kg/m^2)
Nextel 312	0.88	0.15	1200	0.61
Nextel 440	0.87	0.16	1300	0.68

As shown in Table 3, Nextel 312 and 440 have similar emissivity and thermal conductivity properties, meaning that both materials will produce extremely close outer and inner surface temperatures when subjected to the same heating at a given fabric thickness. The predicted maximum outer surface temperature is 505°C, found in Section IV.C, which either of the Nextel fabrics could withstand. The main advantage of using Nextel 440 is the 100°C higher temperature use rating compared to Nextel 312. The Nextel 440 would offer 795 °C temperature margin above the predicted maximum surface temperature, while Nextel 312 would only offer 695°C margin.

To instead evaluate the fabrics by mass properties, the equation for mass of a single layer of fabric is:

$$m_{fabric} = \rho_{fabric} \cdot d \cdot A \tag{15}$$

where d is the fabric thickness and A is the heat shield area. The mass difference per layer between Nextel 440 and Nextel 312 is found by subtracting Eq. (15) evaluated for each material:

$$\Delta m = (\rho_{440} - \rho_{312}) * d_{layer} * A \tag{16}$$

Using 0.81 mm as the fabric thickness per layer [8], and A = 0.407 m^2 it can be calculated that Nextel 440 adds 66 grams per layer more than Nextel 312, or an extra 0.55% of the total allowable system mass per layer. Since both materials provide significant margin over the predicted peak temperature, this additional mass cannot be justified under the RockSat mass constraint. Therefore, Nextel 312 was selected as the ParaShield heat shield material.

C. Combined TPS and Structural Trade Study

1. Trade Study Methodology

Following the selection of Nextel 312 AF-30 as the heat shield fabric, the required fabric thickness and spar material selection are treated as a coupled trade study. Fabric thickness determines the inner surface temperature, T_2, which must remain below the continuous use temperature limit of the spar material that is in direct contact with the fabric. Because this limit varies by material, the required fabric thickness cannot be determined independently of the structural system parameters. For each candidate spar material, the minimum fabric layer count required is found by numerically solving Eq. (13) for increasing layer counts until T_2 falls below 80% of the material temperature limit, providing an extra thermal margin. The minimum spar cross-section is then determined from the governing structural load. The configuration minimizing the total combined TPS and structural mass is then selected.

2. Thermal Analysis

Four spar material candidates were evaluated: aluminum 6061-T6, aluminum 2024-T3, titanium Ti-6Al-4V, and stainless steel 321. The temperatures were found by numerically solving the heat flux model of Eq. (13). A single layer of AF-30 is 0.81 mm thick [8], so the total fabric thickness was an integer multiple of this value. The thermal results are summarized in Table 4.

Table 4: Fabric Thickness and TPS Mass Results

Spar Material Candidate	Layers Required	Thickness of Fabric (mm)	Inner Surface Temperature (°C)	TPS Mass (kg)
Al 6061-T6	59	47.8	119.3	14.65
Al 2024-T3	73	59.1	103.3	18.13
Ti-6Al-4V	7	5.67	279.4	1.74
SS 321	2	1.62	342.6	0.50

As shown in Table 4, the aluminum candidates require an extremely high number of Nextel 312 layers, corresponding to fabric thicknesses of 47.8 mm and 59.1 mm. These are unrealistic results as just the TPS mass alone to support these two aluminum candidates would weigh more than the allowed RockSat payload mass. Both aluminum candidates are therefore eliminated from consideration. Ti-6Al-4V and SS 321 only require 7 layers and 2 layers respectively, with predicted inner surface temperatures within both respective continuous use temperature limits.

3. Structural Analysis

Each radial spar is modeled as a solid square cantilever beam. Four load cases were evaluated to determine the governing minimum cross-section. There was bending from dynamic pressure during entry, lateral bending from the 25 g expected RockSat launch load (L1-002), and axial compression from the 50 g launch load (L1-002). For each load case, the minimum square cross-section side length is found from standard beam theory and applied a safety factor of 1.5. The governing minimum side length is the maximum across all three cases:

$$b_{min} = max\left[\left(\frac{6 \cdot M_{aero} \cdot SF}{\sigma_{yield}}\right)^{1/3}, \left(\frac{6 \cdot M_{lateral} \cdot SF}{\sigma_{yield}}\right)^{1/3}, \sqrt{\frac{F_{axial}/N \cdot SF}{\sigma_{yield}}}\right] \tag{17}$$

The structural analysis found that the minimum cross section always resulted from the 25 g lateral launch load across all spar counts and spar materials.

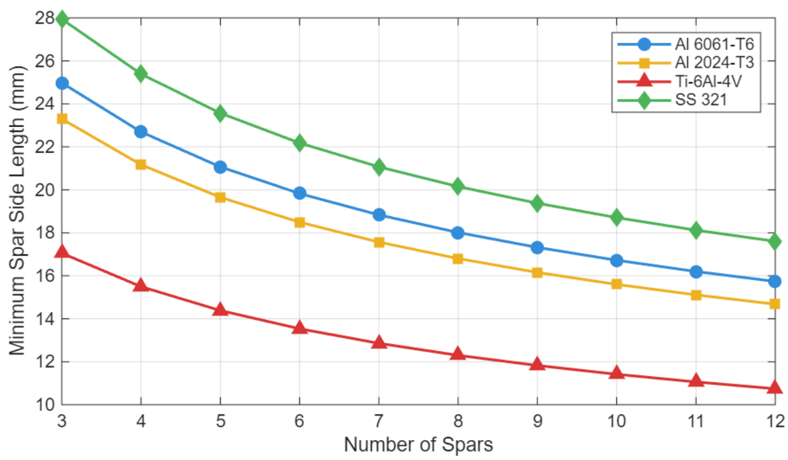

Fig. 9: Minimum Spar Cross Section Length (mm) vs Number of Spars for Each Material

All four spar material candidates exhibit the same behavior in Fig. 9, which is that required cross-sectional area decrease as the number of spars increases. For Ti-6Al-4V the minimum cross-sectional lengths ranged much lower than SS 321, due to the difference in yield strength between the two materials.

4. Spar Count Selection

With Ti-6Al-4V being identified as the lower mass candidate, the necessary spar count is selected by minimizing total system mass, while considering the fabric deflection constraint. The spars divide the circular heat shield surface into equilateral triangular fabric sections that are clamped on either side, and under aerodynamic pressure loading these fabric panels deflect inward. The heat shield is not rigid but rather a fabric membrane, and the flexing effect of the fabric has complex impacts on the resulting heating and forces experienced by the spars, a topic which is explored in Ref. [2]. The required number of spars can then be determined by limiting the allowable deflection of the fabric under aerodynamic loading. This paper established that the fabric panel deflection may not exceed 8.8 mm, which is derived by scaling the deflection to radius requirements established in Ref. [2] to the current ParaShield heat shield radius. It was calculated that none of the current spar counts would violate this requirement given the predicted aerodynamic loading, thus the finalized system mass as a function of spar count was created.

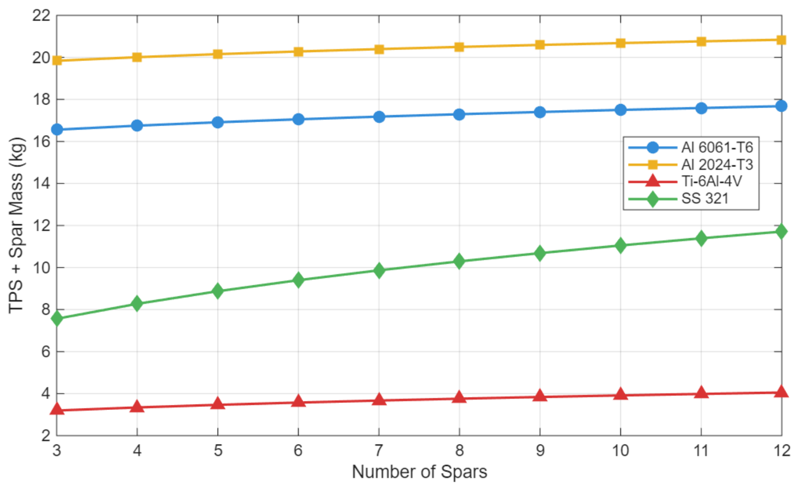

Fig. 10: Total System Mass vs Number of Spars for Each Spar Material

Fig. 10 shows the relationship each spar candidate material had on overall system mass with respect to the number of spars. Ti-6Al-4V is chosen as the spar material due to it having the lowest effect on overall total system mass. However, despite 3 spars being a valid configuration, 3 spars were ultimately not chosen due to the effect odd number of spars have on the lift and drag constants. This behavior for uneven spar counts is analyzed further in Ref. [3].

D. Design Summary

At this point of the paper, all major design choices for geometry, TPS, and radial spars have been made for this scaled model of ParaShield. Future work must be done to finalize additional design specifications.

Table 5: Overall Design Summary

Geometric Parameter	Value
Heat Shield Radius when Deployed	0.36 m
β	219 Pa
TPS Parameter	**Value**
Heat Shield Thickness	5.67 mm
Number of Fabric Layers	7
Heat Shield Material	Nextel 312 AF-30
Structural Parameter	**Value**
Number of Spars	4
Spar Cross Section	Solid Square
Spar Material	Ti-6Al-4V
Minimum Spar Thickness	15.5 mm
TPS Mass	**1.74 kg**
TPS + Radial Spar Mass	**3.34 kg**

The current estimated ballistic coefficient value of 219 Pa is within the ultra-low ballistic coefficient range, but remains higher than the target value of 150 Pa. The main constraint was the limited launch vehicle payload envelope which limited the possible heat shield radius. Additional geometric design work will need to be done to optimize the deployed-to-stowed volume ratio to improve the ballistic coefficient value.

VI. Conclusion

This paper presented the adaptation of the ParaShield ultra-low ballistic coefficient entry vehicle for a suborbital flight test under NASA's RockSat program. The RockSat program introduced a new set of constraints not present in previous ParaShield papers such as the 0.3 m stowed payload envelope, a 12.1 kg mass budget, and a 25 g launch load requirement. Meeting these requirements required refinements to the thermal protection system, structural system, deployment timing window analysis, and a new scaled geometric design.

The results demonstrate that ParaShield shows strong potential to be configured as a flight-ready experimental payload within the RockSat program constraints. There are still several areas of work that remain before this ParaShield design is flight ready. The fabric deflection and panel heating behavior identified in Ref. [2] is a complex phenomenon that warrants a dedicated study into how that may affect ParaShield performance. Additionally, the electrical system design including sensor selection, data acquisition, power management, and autonomous deployment triggering is still being developed by the author. The deployment mechanism, center-of-mass offset and control strategy are also near-term design tasks required before the ParaShield concept can truly be called flight-ready.

Acknowledgments

I would like to thank every student who has contributed to the ParaShield project, from the original MIT design class to the researchers at the University of Maryland whose foundational work made this paper possible. I am especially thankful to Dr. Akin for his unwavering support and guidance throughout my undergraduate education. His extensive knowledge of aerospace systems has served as a continued source of inspiration. Finally, I am grateful for the friendships and mentorship I have found at the Space Systems Laboratory. My time in the lab has been incredibly rewarding.

References

[1] Akin, D. L., "Applications of Ultra-Low Ballistic Coefficient Entry Vehicles to Existing and Future Space Missions," AIAA 2010-1928, *SpaceOps 2010 Conference*, Huntsville, Alabama, April 2010.
DOI:10.2514/6.2010-1928

[2] Magazu, H. K., Lewis, M. J., and Akin, D. L., "Aerothermodynamics of a Parashield Re-Entry Vehicle," *Journal of Spacecraft and Rockets*, Vol. 35, No. 4, pp. 434–441, July–August 1998.
DOI: 10.2514/2.3373

[3] Patten, R. and Hedgecock, J., "A Novel Approach to Spacecraft Re-Entry and Recovery," AIAA 90-0179, *28th Aerospace Sciences Meeting*, Reno, Nevada, January 1990.
DOI: 10.2514/6.1990-179

[4] Akin, D. L., "The ParaShield Entry Vehicle Concept: Basic Theory and Flight Test Development," *Small Satellite Conference*, Utah State Univ., Utah, 1990, URL: https://digitalcommons.usu.edu/cgi/viewcontent.cgi?article=2769&context=smallsat

[5] Pisacane, V.L, and Moore, R.C., *Fundamentals of Space Systems*, Oxford University Press, 1994.

[6] NASA, "Aerothermodynamics Course," *Proceedings of the 2012 NASA Thermal and Fluids Analysis Workshop (TFAWS)*, 2012. URL: https://tfaws.nasa.gov/TFAWS12/Proceedings/Aerothermodynamics%20Course.pdf

[7] NASA Wallops Flight Facility, "RockSat User Guide 2026," Rev. A, Wallops Island, VA, Sep. 4, 2025. URL: https://www.nasa.gov/nasa-rocksat-program/

[8] 3M Company, *3M™ Nextel™ Ceramic Fibers and Textiles: Technical Reference Guide*, 3M Advanced Materials Division, St. Paul, MN, 2021, URL: https://multimedia.3m.com/mws/media/1327055O/3m-nextel-technical-referenceguide.pdf?&fn=14738-Nextel-Technical-Reference-Guide-2021.pdf

[9] Dennis L. Loveless II, "Subsonic and Supersonic Wind Tunnel Evaluation of Ultra Low Ballistic Coefficient Entry" M. S. Thesis, Department of Aerospace Engineering, University of Maryland, 1994